PAPER

Check for updates

Sustainable synthesis of activated porous carbon from lignin for enhanced CO_2 capture: a comparative study of physicochemical activation routes†

Himanshu Patel, [ID] [ab] Amar Mohanty [ID] [ab] and Manjusri Misra [ID] *[ab]

A sustainable and readily available material, lignin protobind 2400, was upcycled to activated porous carbon (APC) compatible with post-combustion CO_2 capture. The effectiveness of the novel two-step physicochemical activation using $KOH + CO_2$ and $ZnCl_2 + CO_2$ was compared with that of the respective physical (only CO_2) and chemical activation (only KOH or $ZnCl_2$). The effect of carbonization conditions (N_2 or CO_2 purging) on the resulting APC properties and CO_2 adsorption performance was studied. The maximum BET surface area of 1480 $m^2 g^{-1}$ and the best CO_2 adsorption capacity of 5.68, 3.66, and 2.67 mmol g^{-1} were observed at 0, 25, and 40 °C/1 bar, respectively. From the precursor to the final product, the APC yield falls within the range of 14.5–40.8 wt%. The APC derived from lignin exhibited better CO_2/N_2 selectivity. The isosteric heat of adsorption for all the APCs remained below 40 kJ mol^{-1}, which suggested a lower energy requirement during the regeneration. The excellent reusability with fluctuations of only 0.51% in the amount of CO_2 adsorbed over ten consecutive adsorption/desorption cycles highlights the APC's outstanding recyclability.

1. Introduction

Climate change is closely tied to the continuous increase in anthropogenic greenhouse gas (GHG) emissions and poses a significant threat to human existence. The energy sector, driven by hefty dependence on fossil fuels, is accountable for 72% of GHGs, with CO_2 contributing 76% to the overall GHG emissions.[1] Despite a noteworthy increase in renewables, fossil fuels are projected to maintain a substantial global dependence of 74% by 2040, underscoring the critical need to decarbonize the energy sector.[2] This highlights the significance of CO_2 as the most crucial greenhouse gas (GHG) contributing to catastrophic events, such as climate change associated with global warming, increased ocean acidity, and rising sea levels. The World Meteorological Organization's report highlights that the socioeconomic consequences of climate change are worsening, with unprecedented GHG concentrations pushing global temperatures perilously closer to critical levels.[3] The primary aim of the Paris Climate Change Agreement is to achieve a 40%

reduction in GHG emissions by 2030.[4] To address the immediate challenges posed by the escalating levels of global CO_2 concentration, there is an ongoing exploration of carbon capture, utilization, and storage (CCUS) as a potential short-term solution to curb the release of this specific greenhouse gas. Fundamentally, carbon capture involves the application of technologies to either directly extract CO_2 from the air/atmosphere or to capture it during the formation process (large point source). Specifically, the removal of CO_2 from a flue gas stream is termed post-combustion CO_2 capture, which can be a cost-effective approach for addressing emissions from current coal and gas-fired power plants, as well as coal-intensive industries, such as cement, oil refineries, chemicals, and steel.[5] Approximately one-third of the existing coal and gas-fired power plants have been constructed in the last decade. Retrofitting these facilities with post-combustion CO_2 capture enables them to remain operational, thereby avoiding the expenses associated with early phase shutdowns.[6]

Several methods such as amine absorption, membrane separation, cryogenic distillation, and physical adsorption have been developed for CO_2 capture from industrial flue gases. The adsorption-based method, utilizing solid adsorbents such as porous aluminosilicate or zeolites, metal organic frameworks, silica gel, and activated porous carbons (APCs), offers excellent performance and energy efficiency compared to other separation techniques.[7,8] In this context, APCs present numerous

a Bioproducts Discovery and Development Centre, Department of Plant Agriculture, University of Guelph, Crop Science Building, Guelph, Ontario N1G 2W1, Canada. E-mail: mmisra@uoguelph.ca

b School of Engineering, University of Guelph, Thornbrough Building, 80 South Ring Road E, Guelph, Ontario N1G 2W1, Canada

† Electronic supplementary information (ESI) available. See DOI: https://doi.org/10.1039/d4ya00305e

advantages over other CO_2 adsorbents. Their affordability, well-developed pore structure, exceptional thermal and chemical stability, heightened efficiency under humid conditions, straightforward surface functionalization, and lower energy requirements during regeneration highlight their significance as CO_2 adsorbents coupled with commendable multi-cyclic stability.[9,10] Presently, large-scale production of APCs predominantly relies on carbon-intensive precursors, such as coal, as well as carbon-neutral alternatives, such as wood and coconut shells.[11] Researchers are exploring economically viable and efficient replacements to mitigate the environmental impact of this sector and fortify the supply chain.[12]

Lignin is the Earth's second most abundant naturally occurring complex organic material. Lignocellulosic wastes (forest and agricultural waste) and pulp paper mills are two potential sources of lignin, generating 225 and 130 Mt of lignin per annum, respectively.[13] Projections indicate that this figure will surge by 225 Mt per year by 2030, driven by the increasing annual production of lignin as a by-product of bioethanol production mandated by the Renewable Fuel Standard (RFS) program aimed at 60 billion gallons of biofuel.[14] Hence, the development of cost-effective valorisation technologies is crucial to ensure the long-term stability and vitality of biorefineries. Traditionally regarded as a low-value waste by-product, recent studies have demonstrated its potential in producing high-value commodities.[15–19] Despite an expanding body of research on the conversion of lignin into commercial commodities, a large fraction of lignin produced by the paper industry is currently incinerated as a low-value fuel for electricity and heat generation (with a value of < $50 per dry ton).[20,21] Less than 2% is used to produce specialty chemicals and other value-added products. The advancement of value-added lignin-derived co-products has the potential to enhance the profitability of second-generation biorefineries and the paper industry by valorising their lignin by-products.

Physical and chemical activation are the most common and extensively studied techniques for producing APCs. Their individual effects on the performance and properties of APCs prepared from a wide range of carbonaceous materials have been investigated extensively. A hybrid synthesis route of physicochemical activation that simultaneously utilizes both physical and chemical activating agents is less explored. Previously, some researchers investigated the effect of physicochemical activation on other applications, such as Cu adsorption,[22] dye (i.e., crystal violet) removal,[23] and CH_4 storage.[24] The effect of physicochemical activation on the CO_2 adsorption performance is even less studied among other applications of APCs. Previous studies have reported the preparation of APC via physicochemical activation using $ZnCl_2 + CO_2$[25] and KOH + CO_2[26,27] for CO_2 adsorption. However, these studies lacked a comparison of the effectiveness of physicochemical activation with the respective physical and chemical reagents used. In our previous study, we compared the CO_2 adsorption performance of APCs derived through physicochemical activation of pine sawdust with those derived through chemical activation (using only KOH) and physical activation (using only CO_2).[28] Physicochemical activation (KOH + CO_2) resulted in APCs with 68% and 586%

more BET surface area compared to APCs derived using only KOH and only CO_2 activation, respectively. However, the CO_2 adsorption capacity of physicochemically activated carbon was 26.5% lower than that of APCs produced using only KOH and 53.3% higher than that of APCs produced using only CO_2 activation. However, a limitation of this study was that it tested only one combination of physical and chemical activating reagents. The results may be significantly different for different combinations and feedstocks.

In this study, the combined effects of chemical activating agents (such as KOH and $ZnCl_2$) and a physical activating agent (CO_2) on the textural properties and CO_2 adsorption performance of the resulting APC were investigated. In addition, we compared the effectiveness of physicochemical activation with that of individual chemical and physical activating agents. The effect of carbonization conditions on APC performance was also studied. Lignin protobind 2400, a sustainable material, was used as a precursor to derive APC for CO_2 capture applications.

2. Experimental

2.1. Feedstock and material

Lignin protobind 2400 (L) was purchased from ALM Private Limited, Hoshiarpur, Punjab, India. The chemical and thermal properties of L have been reported previously.[29] KOH pellets (P250-3) with a purity of ≥85.0%, anhydrous $ZnCl_2$ with a purity of ≥98.0%, and 1 N HCl solution (SA48-1) from Fisher Scientific were used.

2.2. Synthesis of activated porous carbon

A horizontal fixed-bed annealing furnace (Carbolite GERO, GLO 10/11-1G) was used for carbonization and activation. More details on the furnace used have been published elsewhere.[28] APCs were produced by direct activation as well as two-step activation. KOH, $ZnCl_2$, CO_2, and their combinations were used as the activating agents. Based on the type of activating agent used, the activation can be classified into three categories: (i) physical activation using CO_2, (ii) chemical activation utilizing KOH and $ZnCl_2$, and (iii) physicochemical activation using KOH + CO_2 and $ZnCl_2 + CO_2$. Fig. 1 illustrates the methodology followed during the APC preparation. The precursors were dried in a hot-air oven at 80 °C for 24 h, prior to carbonization and/or activation. Lignin protobind 2400 was carbonized at 600 °C, with a heating rate of 7.5 °C min^{-1} of a heating rate and a residence time of 1.5 h in an N_2 atmosphere (at 50 NLPH). The reactor was allowed to cool down naturally and the resulting biochar was labelled as L N. Pore formation via CO_2 mainly occurs via the Boudouard reaction, which is activated above 700 °C.[30] Considering the poor thermal conductivity of the feedstock used and the heat transfer limitations of the reactor housing, all activation experiments were performed at 800 °C. Direct physical activation of lignin protobind 2400 was performed at 800 °C, at a heating rate of 7.5 °C min^{-1}, and with 1.5 h of residence time in a CO_2 atmosphere (at 75 NLPH). The reactor was cooled naturally, and the resulting biochar was

Fig. 1 Methodology followed during the synthesis of activated porous carbon. (L X–Y, where X represents gas purged during carbonization and Y denotes activating agent used; X = N indicates N_2 purging, X = CD indicates CO_2 purging; Y = K denotes KOH activation, Y = CD denotes CO_2 activation, Y = Z denotes $ZnCl_2$ activation, Y = KCD denotes KOH + CO_2 activation, Y = ZCD denotes $ZnCl_2$ + CO_2 activation).

labelled L CD. For all CO_2 related activations, the precursors were heated from room temperature to 800 °C in an N_2 environment (at 50 NLPH). After achieving 800 °C, N_2 purging was stopped, and CO_2 was purged (at 75 NLPH) throughout the holding time of 1.5 h and until the reactor temperature dropped below 700 °C during the natural cool-down cycle. From 700 °C to room temperature, N_2 was purged.

Directly activated APC (*i.e.*, L CD) and biochar (*i.e.*, L N) were pulverized in a ball mill (Fritsch, Pulverisette 5) for 1 h and sieved through 300 μm mesh. Prior to chemical and physico-chemical activation, 25 g of the pulverized precursor was impregnated with 50 g of KOH or $ZnCl_2$, and 150 ml of deionized water was added. The slurry was stirred for 24 h at 500 rpm followed by overnight drying in a hot-air oven at 105 °C. The dried and impregnated samples were activated at 800 °C, with a heating rate of 5 °C min^{-1} for 1.5 h. Adhering KOH or $ZnCl_2$ was removed from the derived APCs *via* hot water washing, followed by acid soaking in 0.1 M HCl, and then further hot water washing until a neutral pH was achieved. The washed APCs were dried at 105 °C for 24 h, labelled, and stored. The yield was calculated based on the initial and final weight differences. The combined yield of the carbonization and activation steps was considered as the APC yield.

L X–Y denotes the lignin protobind 2400 based activated porous carbon. Where X denotes the type of purging gas used during carbonization: X = N indicates carbonization was executed in N_2 and X = CD indicates carbonization was performed in a CO_2 atmosphere. Y denotes the type of activating agent used in the two-step activation process: Y = K indicates KOH is used as an activating agent, Y = CD denotes CO_2 is used as an activating agent, Y = Z means $ZnCl_2$ is used as an activating agent, Y = KCD means KOH + CO_2 is used as the activating agent, and Y = ZCD indicates $ZnCl_2$ + CO_2 is used as the activating agent. For example, L N–KCD represents lignin protobind 2400 based activated carbon derived *via* a two-step activation method from lignin protobind 2400 biochar

prepared in a N_2 atmosphere, followed by activation using KOH + CO_2 as an activating agent. The details of the characterization protocol have been explained elsewhere.[28,31]

3. Results and discussion

3.1. Composition and structural characterization

The elemental compositions of lignin protobind 2400, biochar, and APCs are listed in Table 1. Carbonization significantly increased the carbon content and reduced the hydrogen and oxygen content. Chemical activation using KOH and physical activation using CO_2 produced APC with slightly higher carbon content than biochar. However, chemical activation using $ZnCl_2$ and physicochemical activation (KOH + CO_2 and $ZnCl_2$ + CO_2) significantly reduced the carbon content compared to biochar. Similar trends were observed during physicochemical activation (using KOH + CO_2) of pine sawdust.[28] Compared to the feedstock, the reduced H/C molar ratio for the biochar and APCs indicated that the aromatization reaction was dominant during carbonization and activation.

Scanning electron microscopy (SEM) was utilized to investigate the morphology of the lignin protobind 2400 based APCs. SEM micrographs of all lignin-based APCs are presented in Fig. S1 (ESI†), indicating a blocky and sharp edge morphology. Random cracks and cavities were observed on the external surface. The porous structure and detailed morphology of L N–K were further investigated using transmission electron microscopy (TEM) and high-resolution transmission electron microscopy (HR-TEM). As portrayed in Fig. 2a, the overlapping of multiple carbon sheets resulted in a relatively dense TEM image. The HR-TEM image of L N–K depicted in Fig. 2b shows disordered worm-like micropores randomly distributed on the surface of L N–K, indicating a microporous nature, which was further confirmed by N_2 adsorption isotherms.

Table 1 Elemental composition of the feedstock, biochar, and activated porous carbons

Material	C, wt%	H, wt%	N, wt%	O,[a] wt%	H/C	C/O	H/O
L	63.03 SD = 0.23	6.20 SD = 0.01	1.23 SD = 0.00	29.54 SD = 0.22	1.18	2.85	3.36
L N	84.84 SD = 0.09	2.45 SD = 0.01	1.13 SD = 0.98	11.58 SD = 0.95	0.35	9.77	3.39
L N–K	85.05 SD = 0.30	0.32 SD = 0.03	0.68 SD = 0.02	13.95 SD = 0.27	0.05	8.13	0.37
L CD–K	87.25 SD = 0.63	1.02 SD = 0.01	0.78 SD = 0.01	10.95 SD = 0.62	0.14	10.62	1.49
L N–CD	86.17 SD = 1.79	1.15 SD = 0.10	1.12 SD = 0.13	11.56 SD = 1.95	0.16	9.94	1.59
L CD	85.91 SD = 1.05	0.79 SD = 0.09	1.30 SD = 0.15	12.00 SD = 1.27	0.11	9.55	1.05
L N–KCD	81.86 SD = 1.41	0.51 SD = 0.16	1.22 SD = 0.22	16.41 SD = 1.77	0.07	6.65	0.50
L CD–KCD	81.10 SD = 1.14	1.16 SD = 0.03	1.20 SD = 0.01	16.53 SD = 1.13	0.17	6.54	1.12
L N–Z	76.24 SD = 6.36	0.84 SD = 0.15	0.66 SD = 0.02	22.25 SD = 6.53	0.13	4.57	0.61
L N–ZCD	76.11 SD = 4.67	0.93 SD = 0.13	0.61 SD = 0.04	22.35 SD = 4.80	0.15	5.93	0.90
L CD–Z	80.22 SD = 1.55	1.01 SD = 0.09	0.74 SD = 0.02	18.03 SD = 1.65	0.15	5.93	0.90
L CD–ZCD	80.37 SD = 2.81	1.06 SD = 0.13	0.67 SD = 0.05	17.90 SD = 2.94	0.16	5.99	0.95

[a] By difference. SD = standard deviation.

Raman spectra were recorded to evaluate crystallographic disorders in the carbon structure. Only the key features of the Raman spectra within the Raman shift range of 800–2000 cm^{-1} are highlighted in Fig. 3. Two broad overlapping peaks were deconvoluted using the Fourier–Gaussian peak-fitting method. The first peak, a maxima occurring at ~ 1300 cm^{-1}, represents a defect or disorder in the carbon structure originating from local defects (D-band). The second peak at ~ 1600 cm^{-1} can be attributed to the graphitic crystallites of sp^2 hybridized carbon (G-band). The I_D/I_G ratio is the intensity ratio of the D and G peaks, which quantifies the degree of graphitization. This signifies the ratio of disordered carbon structure to ordered carbon structure. A lower I_D/I_G ratio indicates a more ordered or crystalline carbon structure. Fig. 3k portrays the I_D/I_G ratios of all ten APCs. Physical activation resulted in the most ordered carbon structure morphologically, which is consistent with a previous study using different feedstocks.[28] Chemical or physicochemical activation leads to pronounced deformation of

the aromatic rings, which reduces the degree of graphitization. During activation, $ZnCl_2$ was more reactive towards the aromatic rings of biochar produced in a CO_2 atmosphere than in a N_2 atmosphere. This can be inferred from the higher I_D/I_G ratio for L N–Z than for L CD–Z and L N–ZCD than for L CD–ZCD. Conversely, KOH was more reactive towards aromatic rings of biochar produced in a N_2 atmosphere than in a CO_2 atmosphere. The higher I_D/I_G ratio for L N–K than for L CD–K, L N–KCD and L CD–KCD support this statement.

3.2. Textural properties

The textural properties of the carbonaceous adsorbent significantly affect its CO_2 adsorption performance. Therefore, to evaluate the porosity, N_2 adsorption isotherms were recorded at -196 °C up to a relative pressure of 1.0 bar. Fig. 4a shows the N_2 adsorption isotherms of lignin-based APCs prepared using a wide range of activating agents. For all the samples, a steep rise in N_2 adsorption was observed at $P/P_0 < 0.05$. The rise ranged from 65 to 333 cc g^{-1}, which could be attributed to micropore filling due to better adsorbent–adsorbate interactions at lower pressures.[32,33] Thereafter, beyond $P/P_0 = 0.05$, the N_2 adsorption increased gradually, except for L N–KCD. For L N–KCD, N_2 adsorption continued to rise exponentially up to a P/P_0 of 0.45 and reached a plateau. For all the samples, hysteresis at $P/P_0 > 0.4$ suggested a type IV isotherm according to IUPAC classification. The existence of hysteresis is linked to the capillary condensation of N_2. Hysteresis is a characteristic of mesoporous adsorbents and confirms the presence of micro and mesopores.[34,35] The pore size distribution curve presented in Fig. 4b (and Fig. S2, ESI†) further confirms the microporous and mesoporous nature of all APCs. The figure illustrates pore width maxima occurring at 8.4/9.7/11.1/19.0 Å for L N–K, 9.7/
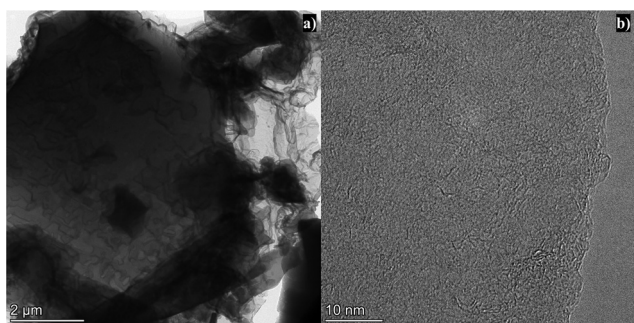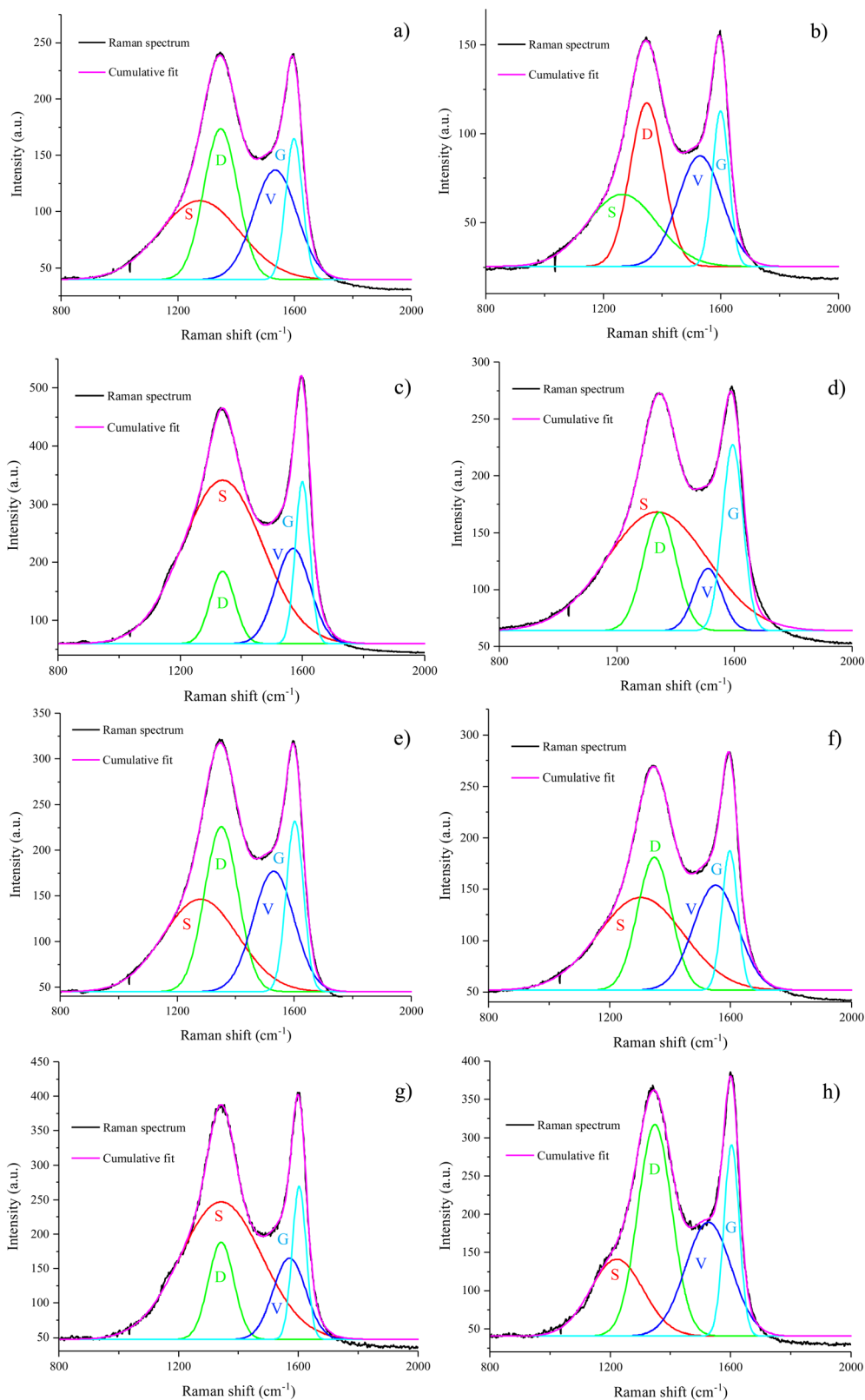

Fig. 2 (a) Transmission electron micrograph and (b) high-resolution transmission electron micrograph of L N–K.
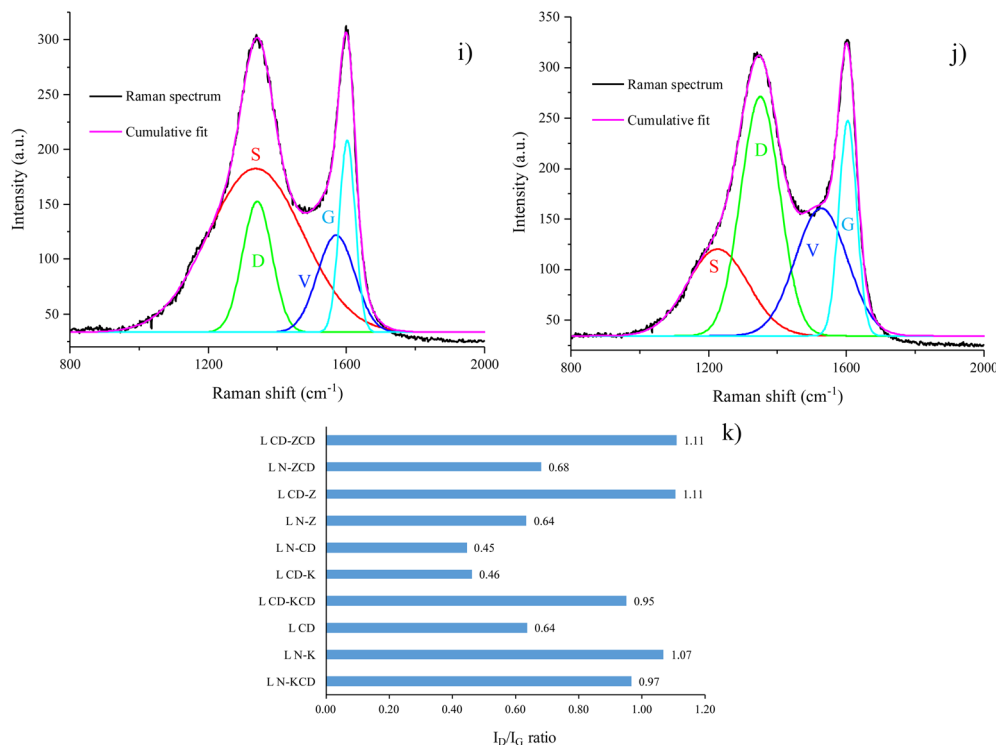
Fig. 3 Curve fitting of Raman spectra (a) L N–K, (b) L CD–K, (c) L N–CD, (d) L CD, (e) L N–KCD, (f) L CD–KCD, (g) L N–Z, (h) L CD–Z, (i) L N–ZCD, (j) L CD–ZCD, and (k) I_D/I_G ratio.

12.1/19.8 Å for L CD–K, 8.4 Å for L N–CD, 19.0 Å for L CD, 8.1/9.2/11.6 Å for L N–KCD, 9.2/19.0 Å for L CD–KCD, 8.4/9.7/19.0 Å for L N–Z, 9.7/19.0 Å for L CD–Z, 8.4/9.7/19.0 Å for L N–ZCD and 8.4/9.2/19.0 Å for L CD–ZCD. For all the APCs, the pore diameter of ~ 8 Å available in the pore size distribution curves was large enough to accommodate CO_2 with a kinetic diameter of 3.3 Å.[36] This is crucial for efficient CO_2 capture. Pore width maxima centred at 19 Å were common in L CD and APCs derived from the secondary activation of L CD, such as L CD–Z and L CD–ZCD. This indicated the absence of a pore-widening effect during secondary chemical activation using $ZnCl_2$ and physicochemical activation using $ZnCl_2 + CO_2$. In contrast, the secondary chemical activation of L CD using KOH resulted in pore widening, and the maxima shifted to 19.8 Å. The pore size distribution curves suggested that the secondary activation of L CD *via* both chemical and physicochemical activation resulted in the formation of additional micropores.

Table 2 lists the yields and key textural properties of the L-based APCs. The conversion yield of the raw biomass to APC ranged within 14.5–40.8 wt%. The highest S_{BET} of 1480 m^2 g^{-1} and maximum total pore volume of 0.737 cm^3 g^{-1} were obtained for the APC produced *via* the physicochemical activation of L N using KOH + CO_2. In contrast, the chemical activation of L N using KOH promoted the formation of micropores, achieving a micro-porosity (φ_{micro}) as high as 97.74%. Physicochemical or chemical treatment of L N led to better porosity than the identical treatment of L CD did. For example, chemical activation of L N using KOH resulted in S_{BET}

of 1108 m^2 g^{-1}, which is considerably higher than that for the chemical activation of L CD using KOH. This could be attributed to the relatively higher processing temperature of L CD (*i.e.*, 800 °C), leading to the formation of a sturdy aromatic structure, which could be less susceptible to further activation. For L N, combined physical and chemical activation (using KOH + CO_2 and $ZnCl_2 + CO_2$) produced better porosity than physical activation (using CO_2) and chemical activation (using KOH and $ZnCl_2$) alone. Compared to KOH activation, physicochemical activation with KOH + CO_2 increased the S_{BET} by 33% and the total pore volume by 31%. However, the S_{BET} and total pore volume were improved by ~ 12% and 10%, respectively, for physicochemical activation using $ZnCl_2 + CO_2$ compared to activation with $ZnCl_2$ only. A similar trend was reported in ref. 24, 28, and 37. For lignin-based APCs, the percentage of micropore volume (f_{micro}) ranged from 81 to 93%, indicating the dominance of micropores. Micropores are desired for better CO_2 capture.

3.3. CO_2 adsorption characteristics

CO_2 and N_2 adsorption isotherms were recorded at 0, 25 and 40 °C up to 1 bar (Table 3). CO_2 uptake values at 0.1–0.15 bar are also listed in Table 3. Low-pressure CO_2 uptake at 0.1–0.15 bar is vital as it represents the realistic partial pressure of CO_2 in the flue gas.[38] Fig. 5a–c demonstrate CO_2 adsorption isotherms at three different temperatures. At 1 bar, saturation in terms of CO_2 uptake was absent for L N–K, L CD–K and L N–KCD, indicating more CO_2 uptake at elevated adsorption pressure.
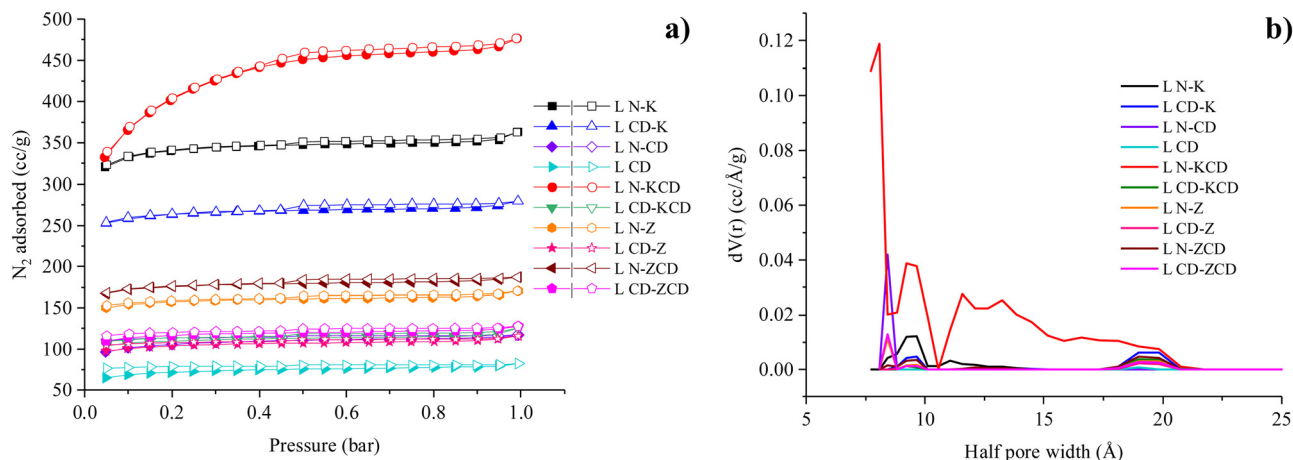
Fig. 4 (a) N_2 adsorption/desorption isotherms of lignin–based activated porous carbons at −196 °C (solid symbols represent adsorption and hollow symbols indicate desorption), and (b) pore size distribution from the NLDFT method using N_2 isotherms at −196 °C.

Table 2 Yield and textural properties of activated carbons derived from lignin protobind 2400 under varied conditions

	Yield, wt%	S_{BET}, m^2 g^{-1}	S_{micro}, m^2 g^{-1}	φ_{micro}, %	R_{avg}, nm	V_T, cm^3 g^{-1}	V_{micro}, cm^3 g^{-1}	f_{micro}, %
L N–KCD	14.54	1480	1383	93.45	0.995	0.737	0.597	81.00
L N–K	28.96	1108	1083	97.74	1.014	0.562	0.515	91.64
L CD	40.82	269	257	95.53	0.946	0.127	0.107	84.25
L CD–K	35.28	844	826	97.87	1.024	0.432	0.400	92.59
L N–CD	35.36	399	385	96.49	0.908	0.181	0.159	87.84
L CD–KCD	30.09	353	338	95.75	1.093	0.193	0.163	84.46
L N–Z	38.93	504	491	97.42	1.045	0.264	0.237	89.77
L CD–Z	31.82	334	322	96.40	1.071	0.180	0.155	86.11
L N–ZCD	37.19	564	551	97.70	1.026	0.290	0.266	91.72
L CD–ZCD	31.82	377	364	96.55	1.051	0.198	0.175	88.38

S_{BET} = specific BET surface area; S_{micro} = micro-pore area using t-plot method; φ_{micro} = micro-porosity, % = $(S_{micro}/S_{BET}) \times 100$; R_{avg} = average pore radius; V_T = estimated at a relative pressure $P/P_0 = 0.99$; V_{micro} = micropore volume estimated using t-plot method; f_{micro} = percentage of micro-pore volume, % = $(V_{micro}/V_T) \times 100$.

This was consistent over the range of tested adsorption temperatures. The absence of hysteresis indicated that CO_2 adsorption followed type I isotherms, which further advocates the microporous nature of the APCs.

Despite having higher S_{BET} for physicochemically activated APC (*i.e.*, L N–KCD), it indicated lower CO_2 adsorption capacity than chemically activated APC (*i.e.*, L N–K). It indicates non-linearity between S_{BET} and CO_2 adsorption capacity, which was commonly observed.[7,28,39,40] Conversely, combined physical and chemical activation using $ZnCl_2 + CO_2$ slightly improved the CO_2 uptake compared to individual physical or chemical activation using CO_2 or $ZnCl_2$, respectively. APCs derived *via* chemical activation using KOH resulted in the highest CO_2 adsorption capacity. The maximum CO_2 adsorption capacity of 5.68 mmol g^{-1} at 0 °C/1 bar was observed for L N–K. At lower adsorption pressure, L CD–K exhibited better CO_2 adsorption than L N–K. However, the CO_2 adsorption capacity of L N–K starts surpassing that of L CD–K above an adsorption pressure of 0.5 bar. The observation was consistent over the range of adsorption temperatures studied. This could be attributed to the superior microporosity of L CD–K as micropores are likely to get occupied first at lower adsorption pressure. Two-step

physical activation yields a slightly better CO_2 adsorption performance than one-step physical activation. Energy penalty during two-step physical activation is yet to be justified by a marginal increase in CO_2 adsorption. From a better CO_2 uptake perspective, the performance of the type of activating agents can be ranked as: KOH > KOH + CO_2 > $ZnCl_2$ + CO_2 > $ZnCl_2$ > CO_2. Table 4 compares the CO_2 adsorption capacity of APCs derived from various biomass precursors.

A linear relationship between CO_2 uptake and textural properties (*i.e.*, S_{BET}, S_{micro}, φ_{micro}, R_{avg}, V_T, V_{micro}, and f_{micro}) is presented in Fig. S3 (ESI†) to better understand the parameters affecting the CO_2 adsorption performance of APC. No clear trend was observed between any of the textural properties and CO_2 uptake. This implied that CO_2 adsorption on the APC surface is affected by multiple parameters.[53]

3.4. Selectivity and heat of adsorption

For practical on-field gas separation applications, better CO_2 uptake along with higher CO_2/N_2 selectivity is desired. A CO_2/N_2 volume ratio of 15 : 85 was assumed, and ideal adsorption solution theory was applied to determine CO_2 over N_2 selectivity at 0, 25, and 40 °C/1 bar. Adsorption isotherms of a single

Table 3 Gas adsorption performance of activated carbons at 0, 25, and 40 °C

| Sample | CO$_2$ adsorption capacity, mmol g^{-1} | | | | | | N$_2$ adsorption capacity, mmol g^{-1} | | | q_{st}, kJ mol^{-1} | CO$_2$/N$_2$ selectivity | | |
| | 1 bar | | | 0.1 (0.15) bar | | | | | | | | | |
	0 °C	25 °C	40 °C	0 °C	25 °C	40 °C	0 °C	25 °C	40 °C		0 °C	25 °C	40 °C
L N–K	5.68	3.66	2.67	1.38 (1.84)	0.72 (1.00)	0.46 (0.66)	0.88	0.52	0.34	25.53	13.52	12.56	12.50
L CD–K	5.16	3.41	2.56	1.73 (2.17)	0.85 (1.12)	0.54 (0.73)	0.75	0.46	0.30	29.99	18.51	16.09	16.14
L N–CD	2.77	2.00	1.57	1.16 (1.40)	0.61 (0.79)	0.40 (0.54)	0.50	0.29	0.18	31.20	18.20	18.10	20.39
L CD	2.64	1.96	1.52	1.07 (1.31)	0.61 (0.79)	0.39 (0.53)	0.47	0.28	0.18	30.31	17.69	17.88	18.79
L N–KCD	4.40	2.87	2.08	0.99 (1.31)	0.52 (0.73)	0.34 (0.48)	0.66	0.40	0.26	24.53	12.97	11.86	11.97
L CD–KCD	2.80	2.02	1.55	1.11 (1.34)	0.61 (0.78)	0.39 (0.53)	0.47	0.28	0.17	30.74	18.21	18.58	19.92
L N–Z	3.06	2.03	1.50	1.00 (1.26)	0.51 (0.67)	0.32 (0.44)	0.49	0.29	0.17	20.29	16.45	15.15	17.17
L CD–Z	2.67	1.84	1.39	0.97 (1.20)	0.50 (0.66)	0.32 (0.43)	0.44	0.26	0.16	32.51	17.71	16.50	17.82
L N–ZCD	3.14	2.04	1.51	0.97 (1.24)	0.50 (0.65)	0.31 (0.43)	0.48	0.29	0.18	29.38	16.53	14.57	15.84
L CD–ZCD	2.73	1.87	1.41	0.98 (1.21)	0.51 (0.67)	0.33 (0.44)	0.45	0.27	0.17	31.10	17.46	16.13	17.17
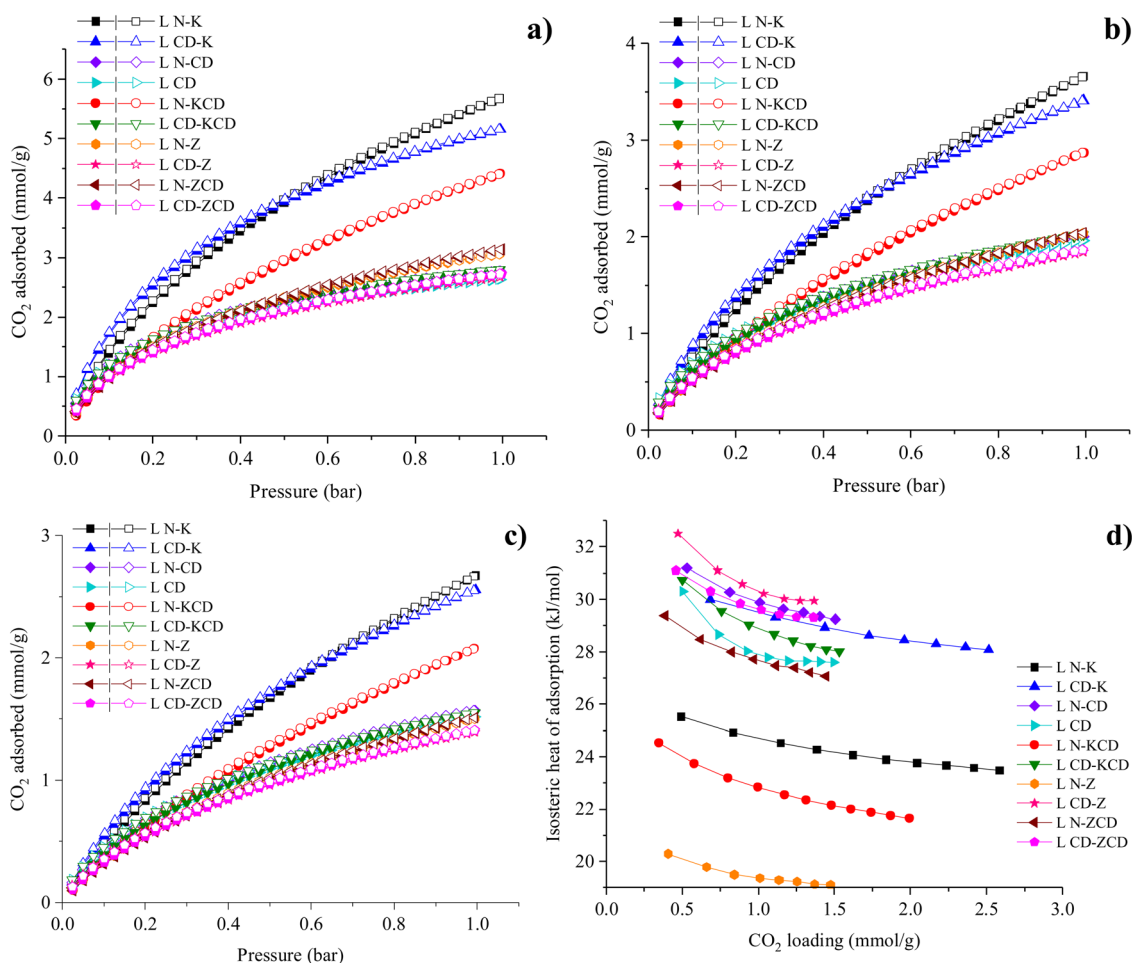
Fig. 5 CO$_2$ adsorption isotherms at (a) 0 °C, (b) 25 °C, and (c) 40 °C (solid symbols represent adsorption, and hollow symbols indicate desorption), and (d) isosteric heat of CO$_2$ adsorption.

component were fitted into the Langmuir–Freundlich isotherm model in eqn (1) and the resulting parameters were fitted to eqn (2).

$$Q = \frac{q_{sat} \times k \times c^n}{1 + k \times c^n} \quad (1)$$

$$S = \frac{q_{CO_2}/q_{N_2}}{p_{CO_2}/p_{N_2}} \quad (2)$$

where, S is the CO$_2$/N$_2$ selectivity, q is the amount of ith gas adsorbed and p is the relative pressure of the ith gas.

Table 4 Comparison of CO_2 adsorption performance of activated porous carbon derived via chemical activation of various biomass precursors

Precursor (P)	Activating agent (AA)	Impregnation ratio (P:AA)	Carbonization (C) & activation conditions (A) (T (°C)/residence time (min))	Yield (wt%)	S_{BET} (m² g⁻¹)	V_t (cm³ g⁻¹)	CO₂ adsorption conditions T (°C)	P (bar)	CO₂ adsorption capacity (mmol g⁻¹)	q_{st} (kJ mol⁻¹)	Selectivity (CO₂/N₂)[e]	Ref.
Bamboo shoot shells[b]	CaCl₂	1:1	C[c]-600/120, A-700/120	—	541	0.24	0/25	1/1	3.14/2.39	35.0	—	41
Bamboo shoot shells + urea[b]	K₂CO₃	1:3	C[c]-500/120, A-800/—	—	1958	0.83	0/25	1/1	7.52/3.60	33.0	14.0	42
Chitosan[a]	KOH	3:2	A-700/60	—	1506	0.64	0/25	1/1	6.91/4.40	32.5	21.0	43
Coconut shells[b]	K₂S₂O₃	1:1	C[c] —, A-700/60	—	1188	0.47	0/25	1/1	5.31/3.59	35.0	20.0	44
Coconut shells[b]	K₂S₂O₈	1:1	C[c]-500/120, A-750/120	—	581	0.26	0/25	1/1	3.77/2.56	39.0	17.0	45
Coconut shells[b]	KOH	1:3	C[c]-500/120, A-600/60	—	1172	0.44	0/25	1/1	6.04/4.23	37.0	22.0	46
Corn cob[b]	KOH	1:3	C[d]-230/480, A-600/60	16.3	2716	0.71	15	1	4.50	24.1	—	47
	ZnCl₂	1:3		18.9	1567	0.48	15	1	3.64	17.7		
	H₃PO₄	1:3		17.3	2314	0.59	15	1	2.95	9.3		
Cotton balls[b]	KOH	1:2	C[c]-500/60, A-700/90	23.3	1381	—	25	1	5.14	—	—	48
Garlic peel[b]	KOH	1:2	C[d]-200/1440, A-800/60	—	1262	0.70	0/25	1/1	4.33/2.82	—	—	49
Lotus seeds[b]	KOH	1:3	C[c]-600/120, A-800/120	—	2230	0.96	0/25	1/1	6.80/3.10	30.4	—	50
Macadamia nutshell[b]	KOH	1:1.7	C[c]-500/120, A-771/150	—	1417	0.75	0/25/40	1/1/1	6.58/3.94/3.15	27.0	—	51
Slash pine[a]	KOH	1:4	A-580/120	19.5	1185	0.35	0/15	1	4.93/3.86	39.7	—	52
Pine sawdust[b]	KOH	1:2	C[c]-600/90, A-800/90	19.89	1319	0.66	0/25/40	1/1/1	6.35/3.82/2.81	24.9	11.8	28
Lignin protobind 2400[b]	KOH	1:2	C[c]-600/90, A-800/90	28.96	1108	0.56	0/25/40	1/1/1	5.68/3.66/2.67	25.5	12.6	Present study

[a] Direct activation. [b] Two-step activation. [c] Pyrolytic carbonization. [d] Hydrothermal carbonization. [e] At 25 °C.
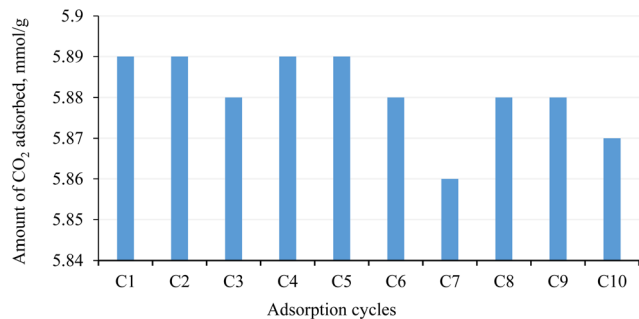
Fig. 6 Multi-cyclic CO_2 adsorption performance of L N–K at 0 °C.

Table 3 lists CO_2/N_2 selectivity for all the APCs, which ranged within 11.9–20.4. A clear trend between selectivity and adsorption temperature was absent. Higher polarizability, quadruple moment, critical temperature, and lower kinetic diameter for CO_2 than N_2, favoured better adsorption of CO_2 on the APC surface.[54] Also, being an electrophilic molecule, CO_2 strongly interacts with the heteroatom-containing functional groups of APCs.

The isosteric heat of adsorption (q_{st}) measures the strength of adhesion between adsorbent and adsorbate, which is linked to the ease of regeneration of the adsorbent. Table 3 lists q_{st} values of all the APCs at lower CO_2 loading, which ranged within $\sim$20–33 kJ mol^{-1}. The q_{st} value is inversely proportional to the energy required during the regeneration of the adsorbent. For all the APCs, $q_{st} < 40$ kJ mol^{-1} indicated that adsorption predominantly occurred *via* physisorption through dipole–quadrupole interaction between CO_2 and the APC surface. Secondary activation of biochar prepared in CO_2 indicated higher CO_2/N_2 selectivity and q_{st} than that of biochar prepared in the N_2 atmosphere. The observation was consistent for all the tested combination of activating agents considered in the study. For example, L N–K *vs.* L CD–K, L N–KCD *vs.* L CD–KCD, L N–Z *vs.* L–CD Z and L N–ZCD *vs.* L CD–ZCD. CO_2 carbonization/activation may have modified the surface chemistry of the material or introduced functional groups, leading to stronger interactions with CO_2 molecules. This enhanced interaction can result in a higher heat of adsorption. A similar trend observed for APCs derived from pine sawdust indicates this effect is not much more feedstock sensitive.[28] Fig. 5d represents variation in q_{st} with CO_2 loading. The elevated q_{st} observed at the minimum CO_2 loading may be explained by a preference for occupying ultrafine pores and/or the adhesion of CO_2 to surface heterogeneity. As CO_2 loading increases, the diminishing trend in the isosteric heat of adsorption can be ascribed to the saturation of strong binding sites. For most of the APCs, a consistently strong correlation with increasing CO_2 loading suggests uniformity in adsorption sites in terms of binding energy. The moderate q_{st} value indicates convenient regeneration, supporting their suitability for multi-cycle CO_2 adsorption applications. Multi-cyclic CO_2 adsorption at 0 °C was executed for the best-performing APC in terms of CO_2 adsorption *i.e.*, L N–K up to 10 cycles. As indicated in Fig. 6, a fluctuation of 0.51% in the amount of CO_2 adsorbed was observed during 10 consecutive adsorption/desorption cycles. The remarkable stability and reusability of L N–K for CO_2

adsorption could be attributed to non-destructive uptake and release. However, its stability towards the actual flue gas scenario has yet to be tested.

As of 2023, approximately 40 commercial CO_2 capture facilities are actively operating worldwide, with a total annual capture capacity exceeding 45 Mt of CO_2. Despite the announcement of over 50 upcoming capture facilities scheduled to commence operations by 2030, declared since January 2022, the current project pipeline only represents roughly one-third of the anticipated requirement for achieving net-zero emissions by 2030. Noteworthy advancements have also been observed in the application of CCUS within the industrial sector. In 2022, several new projects were commissioned, encompassing the integration of CCUS into sectors such as iron, steel, fertilizer, and other chemical production processes. Projections indicate that approximately 25 biomass and waste-fired combined heat and power plants could be responsible for capturing around 30 Mt of CO_2 by the year 2030. Considering the ongoing project pipeline, it is anticipated that by 2030, the annual capture capacity, derived from both new constructions and retrofits, could reach around 90 Mt of CO_2 from hydrogen production, approximately 80 Mt from power generation, and roughly 35 Mt from various industrial facilities, including cement and steel production.[55]

In the wider spectrum, utilization of APC for post-combustion CO_2 capture presents invaluable benefits such as compatibility to current energy systems, easy scalability, and steady operation. APC can be used in packed-bed adsorption systems, known for their simplicity and straightforward scalability. APC derived from green and renewable sources can effectively capture CO_2 emissions from industries heavily reliant on coal, including cement, chemical, oil refineries, and steel. As per the technical report from the National Energy Technology Laboratory (NETL), an adsorbent proves practical and economically viable for CO_2 capture if it demonstrates an isothermal CO_2 adsorption capacity exceeding 3 mmol g^{-1} at 25 °C and 1 bar.[56] The L N–K, as indicated, exhibits an isothermal CO_2 adsorption capacity of 3.66 mmol g^{-1} at 25 °C and 1 bar, signifying its suitability for commercial operations. Along with CO_2 capture applications, the conversion of lignin into a stable form of APC restricts the release of carbon into the atmosphere.

4. Conclusion

Lignin protobind 2400 was converted into a value-added product, activated porous carbon (APC), using combined activating agents KOH + CO_2 and $ZnCl_2$ + CO_2. Also, the effectiveness of the combined physicochemical activation with individual chemical and physical activating agents was compared. Although KOH + CO_2 activation improved the BET surface area by 33% compared to only KOH activation, CO_2 uptake for KOH + CO_2 activation decreased by 23%, compared to only KOH activation. On the other hand, physicochemical activation using $ZnCl_2$ + CO_2 slightly improved the BET surface area as well as CO_2 uptake compared to only $ZnCl_2$ and only CO_2 activation. From a better CO_2 uptake perspective, the performance of this type of activating agent can

be ranked as: $KOH > KOH + CO_2 > ZnCl_2 + CO_2 > ZnCl_2 > CO_2$. Secondary activation of biochar carbonized in the N_2 atmosphere offered a better BET surface area and increased CO_2 uptake compared to that of biochar carbonized in the CO_2 atmosphere. Considerably higher CO_2/N_2 selectivity and isosteric heat of CO_2 adsorption were observed for APC derived from secondary activation of biochar carbonized in a CO_2 environment than in a N_2 environment. The combination of better CO_2 adsorption capacity, lower heat of adsorption, reasonably good CO_2/N_2 selectivity, and excellent reusability/stability of lignin-based APC supported its utilization for post-combustion CO_2 capture.

Nomenclature

GHGs	Greenhouse gases
CCUS	Carbon capture, utilization, and storage
APC	Activated porous carbon
BET	Brunauer–Emmett–Teller
L	Lignin protobind 2400
NLPH	Normal litres per hour
L X–Y	Lignin protobind 2400 based activated porous carbon, where X represents gas purged during carbonization and Y denotes activating agent used; X = N indicates N_2 purging, X = CD indicates CO_2 purging; Y = K denotes KOH activation, Y = CD denotes CO_2 activation, Y = Z denotes $ZnCl_2$ activation, Y = KCD denotes $KOH + CO_2$ activation, Y = ZCD denotes $ZnCl_2 + CO_2$ activation
SD	Standard deviation
SEM	Scanning electron microscopy
TEM	Transmission electron microscopy
HR-TEM	High-resolution transmission electron microscopy
NLDFT	Non-local density functional theory
S_{BET}	Specific BET surface area, $m^2\ g^{-1}$
S_{micro}	Micro-pore area using a t-plot method, $m^2\ g^{-1}$
φ_{micro}	Micro-porosity $(S_{micro}/S_{BET}) \times 100$, %
R_{avg}	Average pore radius, nm
V_T	Estimated at a relative pressure $P/P_0 = 0.99$, $cm^3\ g^{-1}$
V_{micro}	Micropore volume estimated using a t-plot method, $cm^3\ g^{-1}$
f_{micro}	Percentage of micro-pore volume $(V_{micro}/V_T) \times 100$, %
q_{st}	Isosteric heat of adsorption, $kJ\ mol^{-1}$

Author contributions

Himanshu Patel: methodology, validation, formal analysis, investigation, and writing – original draft. Amar Mohanty: conceptualization, resources, supervision, investigation, validation, and writing – review & editing. Manjusri Misra: conceptualization, methodology, funding acquisition, project administration, resources, supervision, investigation, validation, and writing – review & editing.

Data availability

Data for this article, including Raw/processed/metadata files will be available from the corresponding author on reasonable request.

Conflicts of interest

The authors declare that they have no known competing financial interests or personal relationships that could have appeared to influence the work reported in this paper.

Acknowledgements

References

1 CDIAC, Carbon Dioxide Information Analysis Center, 2011.

2 B. P. E. Outlook, London, United Kingdom, 2019.

3 W. M. Organization, WMO Statement on the State of the Global Climate in 2019, 2020.

4 T. R. K. C. Doddapaneni, R. Praveenkumar, H. Tolvanen, J. Rintala and J. Konttinen, *Appl. Energy*, 2018, **213**, 272–284.

5 H. Patel, A. Mohanty and M. Misra, *Renewable Sustainable Energy Rev.*, 2024, **199**, 114484.

6 X. Yuan, J. Wang, S. Deng, M. Suvarna, X. Wang, W. Zhang, S. T. Hamilton, A. Alahmed, A. Jamal and A.-H. A. Park, *et al.*, *Renewable Sustainable Energy Rev.*, 2022, **162**, 112413.

7 L. Rao, S. Liu, L. Wang, C. Ma, J. Wu, L. An and X. Hu, *Chem. Eng. J.*, 2019, **359**, 428–435.

8 A. Mukherjee, J. A. Okolie, A. Abdelrasoul, C. Niu and A. K. Dalai, *J. Environ. Sci.*, 2019, **83**, 46–63.

9 L. Jiang, A. Gonzalez-Diaz, J. Ling-Chin, A. P. Roskilly and A. J. Smallbone, *Appl. Energy*, 2019, **245**, 1–15.

10 Y. Guo, C. Tan, J. Sun, W. Li, J. Zhang and C. Zhao, *Chem. Eng. J.*, 2020, **381**, 122736.

11 G. Singh, K. S. Lakhi, S. Sil, S. V. Bhosale, I. Kim, K. Albahily and A. Vinu, *Carbon*, 2019, **148**, 164–186.

12 A. K. Mohanty, S. Vivekanandhan, O. Das, L. M. Romero Millán, N. B. Klinghoffer, A. Nzihou and M. Misra, *Nat. Rev. Methods Primers*, 2024, **4**, 19.

13 J. Becker and C. Wittmann, *Biotechnol. Adv.*, 2019, **37**, 107360.

14 U. S. EPA, United States Environ. Prot. Agency.

15 Z. Wu, J. Zou, Y. Zhang, X. Lin, D. Fry, L. Wang and J. Liu, *Chem. Eng. J.*, 2022, **427**, 131547.

16 P. Sirous-Rezaei, D. Creaser and L. Olsson, *Appl. Catal., B*, 2021, **297**, 120449.

17 L. Yu, L. Liang, I. Bajaj, K. Seabright, D. J. Keffer, I. N. Ivanov, H. Chen, S. Dai, A. J. Ragauskas, C. T. Maravelias and D. P. Harper, *Carbon*, 2023, **213**, 118285.

18 Y.-Y. Wang, C. E. Wyman, C. M. Cai and A. J. Ragauskas, *ACS Appl. Polym. Mater.*, 2019, **1**, 1672–1679.

19 J. Zhang, L. Yu, Z. Wang, Y. Tian, Y. Qu, Y. Wang, J. Li and H. Liu, *J. Chem. Technol. Biotechnol.*, 2011, **86**, 1177–1183.

20 M. Y. Balakshin, E. A. Capanema, I. Sulaeva, P. Schlee, Z. Huang, M. Feng, M. Borghei, O. J. Rojas, A. Potthast and T. Rosenau, *ChemSusChem*, 2021, **14**, 1016–1036.

21 H. Luo and M. M. Abu-Omar, *Encyclopedia of Sustainable Technologies*, 2017, vol. 3, pp. 573–585.

22 D. V. Cuong, N.-L. Liu, V. A. Nguyen and C.-H. Hou, *Sci. Total Environ.*, 2019, **692**, 844–853.

23 D. V. Cuong and C.-H. Hou, *J. Taiwan Inst. Chem. Eng.*, 2022, **139**, 104533.

24 K. Adlak, R. Chandra, V. K. Vijay and K. K. Pant, *J. Anal. Appl. Pyrolysis*, 2021, **155**, 105102.

25 S. Balou, S. E. Babak and A. Priye, *ACS Appl. Mater. Interfaces*, 2020, **12**, 42711–42722.

26 A. D. Igalavithana, S. W. Choi, P. D. Dissanayake, J. Shang, C.-H. Wang, X. Yang, S. Kim, D. C. W. Tsang, K. B. Lee and Y. S. Ok, *J. Hazard. Mater.*, 2020, **391**, 121147.

27 J. Serafin, B. Dziejarski, X. Vendrell, K. Kiełbasa and B. Michalkiewicz, *Biomass Bioenergy*, 2023, **175**, 106880.

28 H. Patel, H. Weldekidan, A. Mohanty and M. Misra, *Carbon Capture Sci. Technol.*, 2023, 100128.

29 S. Sahoo, M. Ö. Seydibeyoğlu, A. K. Mohanty and M. Misra, *Biomass Bioenergy*, 2011, **35**, 4230–4237.

30 N. A. Ahmad, K. A. Al-attab, Z. A. Zainal and P. Lahijani, *Bioresour. Technol. Rep.*, 2021, **15**, 100785.

31 H. Weldekidan, H. Patel, A. Mohanty and M. Misra, *Carbon Capture Sci. Technol.*, 2024, **10**, 100149.

32 S. Rani, E. Padmanabhan and B. K. Prusty, *J. Pet. Sci. Eng.*, 2019, **175**, 634–643.

33 W. Wu, C. Wu, G. Zhang, J. Liu, Y. Li and G. Li, *Fuel*, 2023, **332**, 126107.

34 S. Charola, H. Patel, S. Chandna and S. Maiti, *J. Cleaner Prod.*, 2019, **223**, 969–979.

35 J. Rouquerol, D. Avnir, C. W. Fairbridge, D. H. Everett, J. M. Haynes, N. Pernicone, J. D. F. Ramsay, K. S. W. Sing and K. K. Unger, *Pure Appl. Chem.*, 1994, **66**, 1739–1758.

36 Y.-S. Bae and C.-H. Lee, *Carbon*, 2005, **43**, 95–107.

37 K. Kiełbasa, Ş. Bayar, E. A. Varol, J. Sreńscek-Nazzal, M. Bosacka and B. Michalkiewicz, *Ind. Crops Prod.*, 2022, **187**, 115416.

38 B. Ashourirad, P. Arab, T. Islamoglu, K. A. Cychosz, M. Thommes and H. M. El-Kaderi, *J. Mater. Chem. A*, 2016, **4**, 14693–14702.

39 M. Singh, N. Borkhatariya, P. Pramanik, S. Dutta, S. K. Ghosh, P. Maiti, S. Neogi and S. Maiti, *J. CO₂ Util.*, 2022, **60**, 101975.

40 B. Zhao, M. Borghei, T. Zou, L. Wang, L.-S. Johansson, J. Majoinen, M. H. Sipponen, M. Österberg, B. D. Mattos and O. J. Rojas, *ACS Nano*, 2021, **15**, 6774–6786.

41 W. Wu, C. Wu, G. Zhang and J. Liu, *J. Anal. Appl. Pyrolysis*, 2022, **168**, 105742.

42 W. Wu, C. Wu, J. Liu, H. Yan, G. Zhang, G. Li, Y. Zhao and Y. Wang, *Fuel*, 2024, **363**, 130937.

43 J. Shao, J. Wang, Q. Yu, F. Yang, M. Demir, O. C. Altinci, A. Umay, L. Wang and X. Hu, *Sep. Purif. Technol.*, 2024, **333**, 125891.

44 J. Bai, J. Shao, Q. Yu, M. Demir, B. Nazli Altay, T. Muhammad Ali, Y. Jiang, L. Wang and X. Hu, *Chem. Eng. J.*, 2024, **479**, 147667.

45 C. Liu, Y. Zhi, Q. Yu, L. Tian, M. Demir, S. G. Colak, A. A. Farghaly, L. Wang and X. Hu, *ACS Appl. Nano Mater*, 2024, **7**(5), 5434–5441.

46 J. Yang, L. Yue, X. Hu, L. Wang, Y. Zhao, Y. Lin, Y. Sun, H. DaCosta and L. Guo, *Energy Fuels*, 2017, **31**, 4287–4293.

47 A. Sarwar, M. Ali, A. H. Khoja, A. Nawar, A. Waqas, R. Liaquat, S. R. Naqvi and M. Asjid, *J. CO₂ Util.*, 2021, **46**, 101476.

48 H. Patel, H. Mangukiya, P. Maiti and S. Maiti, *J. Cleaner Prod.*, 2020, 125738.

49 G. Huang, G. Liu, X. Wu and J. Cai, *New Carbon Mater.*, 2019, **34**, 247–257.

50 G. Singh, K. S. Lakhi, K. Ramadass, C. I. Sathish and A. Vinu, *ACS Sustainable Chem. Eng.*, 2019, **7**, 7412–7420.

51 C. Wu, G. Zhang, J. Liu, H. Yan and Y. Lv, *Int. J. Energy Res.*, 2022, **46**, 17204–17219.

52 M. B. Ahmed, M. A. H. Johir, J. L. Zhou, H. H. Ngo, L. D. Nghiem, C. Richardson, M. A. Moni and M. R. Bryant, *J. Cleaner Prod.*, 2019, **225**, 405–413.

53 C. Wu, J. Liu, Y. Wang, Y. Zhao, G. Li and G. Zhang, *Sep. Purif. Technol.*, 2024, **329**, 125188.

54 P. Pramanik, H. Patel, S. Charola, S. Neogi and S. Maiti, *J. CO2 Util.*, 2021, **45**, 101450.

55 I. 2023, Tracking Clean Energy Progress 2023, Paris, 2023.

56 H. W. Pennline, *Sorbent Research for the Capture of Carbon Dioxide*, 2016.